

---

# LEARNING THE RULES OF CELL COMPETITION WITHOUT PRIOR SCIENTIFIC KNOWLEDGE

---

Christopher J. Soelistyo<sup>1,2</sup>

Giulia Vallardi<sup>2</sup>

Guillaume Charras<sup>1,3,4</sup>

Alan R. Lowe<sup>1,2,4,5\*</sup>

<sup>1</sup>Institute for the Physics of Living Systems

<sup>2</sup>Department of Structural and Molecular Biology

<sup>3</sup>Department of Cell and Developmental Biology

<sup>4</sup>London Centre for Nanotechnology

University College London, Gower St, London, WC1E 6BT, UK

<sup>5</sup>The Alan Turing Institute

Euston Rd, London NW1 2DB, UK

## ABSTRACT

1 Deep learning is now a powerful tool in microscopy data analysis, and is routinely used for image  
2 processing applications such as segmentation and denoising. However, it has rarely been used to  
3 directly learn mechanistic models of a biological system, owing to the complexity of the internal  
4 representations. Here, we develop an end-to-end machine learning model capable of learning the rules  
5 of a complex biological phenomenon, cell competition, directly from a large corpus of time-lapse  
6 microscopy data. Cell competition is a quality control mechanism that eliminates unfit cells from  
7 a tissue and during which cell fate is thought to be determined by the local cellular neighborhood  
8 over time. To investigate this, we developed a new approach ( $\tau$ -VAE) by coupling a variational  
9 autoencoder to a temporal convolution network to predict the fate of each cell in an epithelium.  
10 Using the  $\tau$ -VAE's latent representation of the local tissue organization and the flow of information  
11 in the network, we decode the physical parameters responsible for correct prediction of fate in  
12 cell competition. Remarkably, the model autonomously learns that cell density is the single most  
13 important factor in predicting cell fate – a conclusion that has taken over a decade of traditional  
14 experimental research to reach. Finally, to test the learned internal representation, we challenge the  
15 network with experiments performed in the presence of drugs that block signalling pathways involved  
16 in competition. We present a novel discriminator network that, using the predictions of the  $\tau$ -VAE,  
17 can identify conditions which deviate from the normal behaviour, paving the way for automated,  
18 mechanism-aware drug screening.

## 19 Introduction

20 Cell competition is a phenomenon that results in the elimination of less fit cells from a tissue – a critical process in  
21 development, homeostasis and disease [1]. The viability of loser cells depends strongly on context: when they are  
22 cultured alone, they thrive, but when in a mixed population, they are eliminated by cells with greater fitness (**Fig 1a**). In  
23 development, competition acts as a quality control mechanism and also participates in pattern formation [2]. In cancer,  
24 competition has been hypothesised to underlie the heterogeneity in cell types present in tumours and promote the  
25 emergence of the most aggressive cells [3]. However, the rules that determine individual cell fate are poorly understood.  
26 A number of mechanisms of cell competition have been identified to date involving either biochemical competition (for

---

\*To whom correspondence should be addressed: a.lowe@ucl.ac.uk

27 example through competition for pro-survival growth factors) or mechanical competition (for example a fast growing  
28 clone compresses cells in a slow growing clone, which results in cell extrusion for the now denser slow growing clone)  
29 [1, 4, 5]. While competition was initially thought to take place only at the interface between cell lineages, the discovery  
30 of mechanical competition revealed that this is not necessarily the case and that extrusion may take place several cell  
31 diameters away from this interface [4]. Over a decade of experimental research has suggested that local cell density  
32 is a key determinant of cell fate in mechanical competition [6, 4, 7, 8, 9]. However, the vast majority of studies have  
33 examined mechanisms of competition at the population level, owing to the difficulty of quantitatively describing the  
34 time evolution of an entire system of cells. As such, our understanding of the cell-scale topological and physical  
35 parameters that determine fate in competition remains incomplete.

36 In this study, we sought to examine a new scientific paradigm – using Artificial Intelligence (AI) to uncover the  
37 determinants of cell fate directly from a large corpus of time-lapse microscopy data. Specifically, we sought to explore  
38 the possibility of learning an interpretable and predictive model of competition using a minimally-supervised and  
39 unbiased approach.

40 Recent studies have shown that machine learning (ML) is adept at uncovering complex patterns in microscopy data. In  
41 conventional feature engineering approaches, prior knowledge is incorporated into a model by choosing features that  
42 represent the system, for example, by measuring image properties or adding relevant fluorescent cell signalling reporters.  
43 This has recently been used, with ML-enabled dimensionality reduction, to study transitions in human pluripotent  
44 stem cell populations [10]. However, choosing appropriate measurements becomes increasingly difficult with more  
45 complex features such as describing the local topology of tissues comprising multiple cell types and varying degrees  
46 of epithelialisation. One promising method is the use of unsupervised deep learning methods, such as variational  
47 autoencoders (VAE, [11]). A VAE learns a probabilistic approximation of the underlying distribution of data, meaning  
48 that the latent representation can be used as descriptive features of the system. Several recent studies have utilised  
49 autoencoders to encode complex cell shapes and other visual features in an interpretable manner [12, 13, 14, 15].  
50 However, these studies have typically been performed on sparse, isolated cells and usually as single observations in  
51 time. Other models have attempted to explicitly incorporate time. For example, a recurrent neural network was used to  
52 predict lineage choices in hematopoietic stem cells [16]. However, this architecture does not lend itself to introspection  
53 and therefore does not directly provide any interpretable insight into the biology.

54 Here, we sought to learn a model of cell behaviour directly from time-lapse image data. We expand upon the use  
55 VAEs to encode cell shape and incorporate local tissue topology as well temporal features, to learn an explainable  
56 model of a complex, physiologically important biological phenomenon, cell competition. Finally, we introduce a novel  
57 discriminator network, that uses this learned model to identify drugs that affect the underlying mechanism of cell  
58 competition.

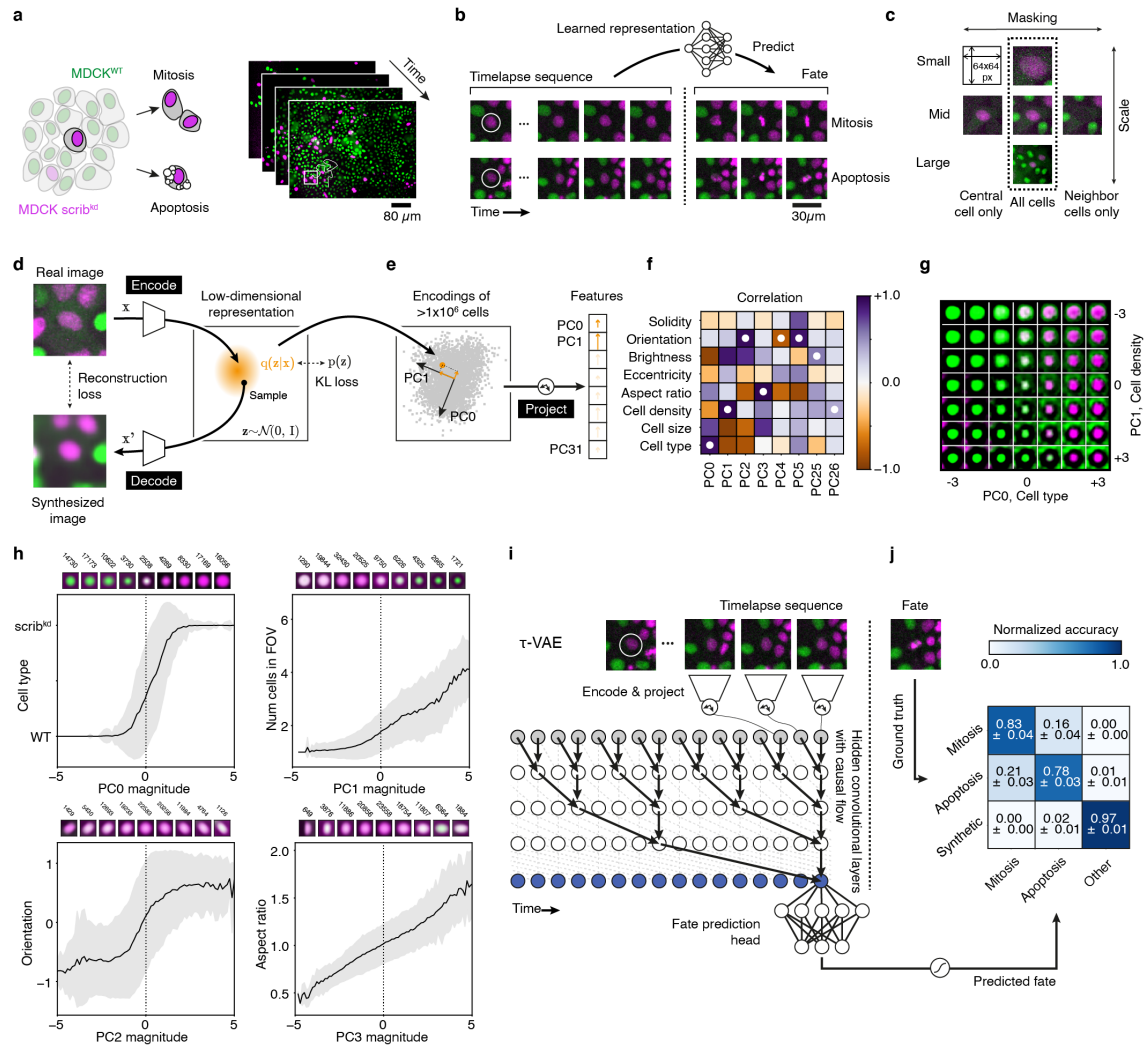
## 59 Results and Discussion

### 60 Data acquisition and training data

61 We used a well-described model of cell competition consisting of co-cultures of mammalian MDCK wild-type  
62 (MDCK<sup>WT</sup>) and a variant expressing an shRNA targeting the polarity protein *scribble* that can be induced to become  
63 mechanical loser cells by addition of tetracycline (*scrib<sup>kd</sup>*) [17]. To differentiate *scrib<sup>kd</sup>* from their MDCK<sup>WT</sup> counter-  
64 parts, we expressed nuclear markers fused to different fluorescent proteins (e.g. H2B-GFP for MDCK<sup>WT</sup>, and H2B-RFP  
65 for *scrib<sup>kd</sup>*). Cells were seeded in different ratios, and then, using automated time-lapse microscopy we followed the  
66 evolution of the competition over periods of 80 h, taking images at 4 min intervals. We collected 111 independent  
67 movies, totaling 7,768 hours of competition experiments (**Fig 1a**).

68 From this dataset, we extracted single-cell trajectories, making sure that we could observe the entire lifespan of each  
69 cell including its fate (either mitosis or apoptosis). To do this, we segmented the time-lapse image data using a fully  
70 convolutional residual U-Net [18], then used a dedicated convolutional neural network (CNN) to classify each nucleus  
71 into one of five states (interphase, prophase, metaphase, anaphase or apoptotic) based on image features [8]. Then,  
72 we tracked all cells over time [19]. Next, we classified the fate of each track as either mitotic, apoptotic or unknown  
73 using a dedicated cell fate classification network (**Fig 1b, Supplementary Information**). We discarded trajectories  
74 with an unknown fate. We manually verified all apoptotic trajectories and a subset of mitotic trajectories to confirm that  
75 the fate labels could be used as ground truth for the purposes of training a model. In total we acquired 36,062 mitotic  
76 and 2,225 apoptotic trajectories, distributed across the two cell types (**Supplementary Information**). Since we do not  
77 know *a priori* what information is required to predict cell fate, we extracted glimpses [20] (**Fig 1c**) which capture three  
78 different spatial scales of the neighbourhood surrounding the cell of interest (Small, Mid and Large, corresponding to  
79 21×21 μm, 42×42 μm and 84×84 μm FOV respectively) but contain the same number of pixels (64 × 64 px). Further,  
80 for the mid-scale view, we also applied masking (using segmentation masks) to artificially remove either the central

Learning the rules of cell competition without prior scientific knowledge



81 cell or the neighbors from the image data (**Fig 1c**) to test which representation was most salient. These five datasets  
82 could then be used to determine the best performing models and determine where the information necessary for fate  
83 prediction is contained.

#### 84 **An explainable model for cell fate prediction from image sequences**

85 Having acquired a large training set, we next designed a machine learning framework to learn the features of a single  
86 cell and its neighbourhood over time, which act as strong predictors of cell fate. One of the design goals of this  
87 system was to have minimal human prior insight integrated into the model. First, we sought to learn an interpretable  
88 representation of the image data in an unsupervised manner. We trained a variational autoencoder ( $\beta$ -VAE, **Methods**,  
89 [11, 21]) to learn a compact latent representation of cell image data using 1.2 million different images of individual  
90 cells and their first neighbours (**Fig 1d**). The  $\beta$ -VAE learns a low dimensional representation of the image data using  
91 a probabilistic encoder. This low dimensional representation (bottleneck) should encode the image in a minimal  
92 number of parameters, in the same way that a human operator might describe the image in terms of the cell type,  
93 orientation of cells, local neighborhood and so forth. Next, a decoder attempts to reconstruct the real image using this  
94 low dimensional representation. The objective function guides the  $\beta$ -VAE to learn a representation of the image data  
95 which is expressive enough to reconstruct the original features, but where each of the latent dimensions are independent  
96 and interpretable. We modified the training objective to linearly increase the *capacity* of the bottleneck of the  $\beta$ -VAE  
97 during training. At low capacities the network is forced to prioritise matching the approximate posterior to the exact  
98 posterior distribution. At higher capacities, the network prioritises the quality of the reconstruction. During training the  
99  $\beta$ -VAE first learns to represent gross level information such as cell type, before features such as cell shape and local  
100 topology (**Supplementary Information**).

101 By encoding a large set of images we were able to perform Principal Component Analysis (PCA) in the latent space,  
102 which yields linear features that explain the variance in the entire dataset (discussed later, **Fig 1e-h**). We use these  
103 principal components (PCs) as the inputs for making predictions.

104 Next, we built a prediction network that utilises the temporal sequence of images of each single-cell trajectory to output  
105 cell fate. Based on current biological knowledge, we reasoned that the biochemical commitment to apoptosis or division  
106 occurs hours before we observe the fate, so we trimmed each trajectory to remove observations that show recognizable  
107 morphological features of mitosis (such as DNA condensation in prometaphase and alignment of chromosomes during  
108 metaphase) or apoptosis (such as DNA fragmentation) (**Supplementary Information**). As such, the prediction network  
109 is forced to use only features from the time evolution of the interphase cell and its neighbours to make a prediction  
110 about the fate. Next, we encoded and projected each of these movies using the  $\beta$ -VAE (**Fig 1e**), and passed them to a  
111 temporal convolution network (TCN, [22]).

112 The TCN uses *causal convolutions* to ensure the prediction at time  $t$  is only dependent on information from  $x_{t-r} \dots x_t$ ,  
113 where  $r$  is the receptive field (equivalent to a window of time before an event,  $\sim 8.5$  h in this case) of the TCN  
114 (**Supplementary Information**). The output of the TCN is connected to a dedicated prediction head, a densely  
115 connected network with three outputs corresponding to “apoptosis”, “mitosis” and “other”. A final softmax activation  
116 yields the prediction of the full network. Overall, The TCN acts as a sequence classifier, taking a sequence of  
117 observations of a single-cell in interphase and returning a prediction for the cell fate, without ever observing the fate  
118 (**Fig 1i**). We refer to the variational encoder and projector coupled to the temporal convolution network as a  $\tau$ -VAE. In  
119 training the  $\tau$ -VAE, we supplemented the real data corresponding to mitotic and apoptotic classes, with a dynamically  
120 generated “synthetic” class to simulate trajectories which were neither apoptotic nor mitotic, corresponding to the “other”  
121 output class (**Methods, Supplementary Information**). In doing so, the prediction problem becomes a multiclass  
122 problem as opposed to a binary problem, thus ensuring that the model learns the features of both apoptotic and mitotic  
123 events. This is important as we do not want the model to learn only the features of mitosis, and predict apoptosis by  
124 exclusion, or *vice versa*.

125 We tested the five different representations of the image data (**Fig 1c**) as input to the prediction network. In all  
126 representations the image data was limited to the same number of pixels, but comprised either different spatial scales  
127 or lacked information about either the central cell or the neighbors. We trained the  $\tau$ -VAE network and measured  
128 the accuracy by comparing the predicted fate with the ground truth fate on a set of unseen test data consisting of 300  
129 trajectories. For each dataset, we split the data by the cell type (MDCK<sup>WT</sup> or scrib<sup>kd</sup>) and calculated separate confusion  
130 matrices to ensure that there was no systematic bias in the predictions. To account for any potential bias in the testing  
131 set, we performed  $k$ -fold cross-validation ( $k = 10$ ) on each model (**Methods**), randomly choosing a subset of training  
132 and testing data in each validation. Overall, the best performing networks used only the central cell region to predict the  
133 fate, with an average fate prediction  $F_1$ -score of  $0.87 \pm 0.02$ , across both cell types as shown in the confusion plots (**Fig**  
134 **1j, Supplementary Information**). For reference, a TCN trained using a set of human chosen image features (those  
135 shown in **Fig 1f**) achieves a lower  $F_1$ -score of 0.71, and is particularly poor at identifying apoptosis, with an accuracy



136 of 0.49. This demonstrates that the  $\beta$ -VAE is able to capture more salient image features, enabling a more accurate  
137 fate prediction, by learning them directly from the distribution of the data. We used the best performing network  
138 ("Small View, All Cells" model, *i.e.* cropped to the central cell at the highest magnification) for all further analyses. We  
139 concluded that the  $\tau$ -VAE network is able to accurately predict the cell fate based only on the interphase local tissue  
140 organization alone, having learnt features directly from the image data to enable this task. Next, we sought to introspect  
141 the model and to assign meaningful semantic labels to the learnt features.

## 142 **Interpreting the model**

143 The goal of the  $\tau$ -VAE network is to learn an end-to-end model that requires minimal input from experts to predict  
144 the fate of cells in competition. The implicit hypothesis is that there is sufficient information in the observations of  
145 local tissue organization to enable this prediction. Having determined that our approach is able to accurately predict the  
146 fate of cells in a competitive system, we sought to interrogate the learnt features of the  $\beta$ -VAE. In contrast to other  
147 approaches, we do not perform feature engineering to select parameters that define the problem (such as cell density,  
148 number of neighbours, etc), but rather, we extract these automatically and directly from the data, based on the latent  
149 space of the  $\beta$ -VAE. We used several different approaches to interpret the model.

150 **Assigning physical parameters to the latent features** Since the training objective of the  $\beta$ -VAE encourages a  
151 continuous, but disentangled internal representation of the image data, we sought to assign meaningful semantic labels  
152 to those latent variables. Analysis of the latent features revealed that some parameters show covariance – for example,  
153 in the dataset, there is a correlation between cell type and nuclear area, since  $\text{scrib}^{\text{kd}}$  cells tend to have larger nuclei  
154 than MDCK<sup>WT</sup> cells. Therefore, we performed PCA on the latent space ( $\mathbf{z} \in \mathbb{R}^{32}$ ) yielding 32 principal components  
155 ordered by the magnitude of the variance explained by the component. We analysed the correlation of the components  
156 with parameters that could be measured from the images (**Fig 1g**). Inspecting these components shows that the first  
157 two (PC0 and PC1) account for 26.9% of the variability of the data, and seem to represent cell type and cell density  
158 (number of cells visible in the glimpse) respectively (**Fig 1f-h**). Component PC2 encodes an orientation parameter  
159 of the central nucleus, while component PC3 encodes nuclear aspect ratio (**Fig 1g-h**). Higher principal components,  
160 such as PC25 encode parameters such as fluorescence intensity of H2B-GFP/RFP but the correlation coefficient is  
161 weaker. We confirm these assignments by sampling images from the dataset with various values for these components  
162 (**Supplementary Information**). Later components broadly enable the network to encode the arrangement and identity  
163 of cells in the local neighbourhood (**Supplementary Information**). Strikingly, projecting the  $\beta$ -VAE latent space  
164 enabled us to learn an explainable model of the local tissue organization of cells in a completely unsupervised manner.  
165 Next, we sought to investigate the role of these principal components over time in the prediction of cell fate.

166 **Feature ablation studies to determine the minimal information required for prediction** To determine the mini-  
167 mal information required for cell fate prediction, we removed individual components in a systematic manner (replacing  
168 them with Gaussian noise at all time steps) and calculated the performance of the network after each component removal.  
169 Ablated networks were ranked according to their effect on the prediction accuracy. Through multiple iterations, we  
170 found that a single component (PC1 - nuclear area/cell density) could be used to predict cell fate with  $43 \pm 2\%$  accuracy  
171 – significantly higher than random chance assuming an equal probability of choosing any fate (33.33%, **Fig 2a**). In  
172 the ablation approach, PC1 was the last component to be removed, suggesting the single highest contribution to the  
173 prediction accuracy. The ablation study reveals that the top five components (PC1, PC5, PC26, PC3, PC26) account for  
174 64% of the prediction accuracy, with the remaining 27 components contributing a further 36%. Importantly, when all  
175 inputs are replaced by noise, all fates are predicted with equal probability, suggesting no inherent bias toward any fate  
176 in the network. Remarkably, this suggests that, in line with our current understanding of mechanical cell competition  
177 stemming from nearly a decade of experimental studies [17, 7, 23, 8, 9], our model has autonomously learnt that cell  
178 density is a strong predictor of cell fate, directly from the data with no expert input.

179 **Timescales of predictions and feature saliency to visualize network attention** Since the TCN is able to output a  
180 prediction after every additional time step, we can use the prediction head (**Fig 1i**) to visualize the time evolution of the  
181 prediction (**Fig 2b-c**). Across all of the data, we find that for the  $\text{scrib}^{\text{kd}}$  cells, the  $\tau$ -VAE network predicts apoptosis  
182 early (up to 8h before an event) and mitosis late ( $\sim 2$ h before an event, **Supplementary Information**). Further, we  
183 can inspect the magnitude and contribution of each principal component to the prediction. In general, we found that  
184 PC1 (cell density) was often much larger in those trajectories undergoing apoptosis. To assess the model's use of  
185 components to make predictions, we utilise the error gradients during backpropagation in the network to calculate  
186 the saliency (**Methods**, [24]). Feature saliency is a method to determine which features of the input contribute most  
187 significantly to the classification accuracy of the  $\tau$ -VAE. We computed this in two ways (i) PC feature saliency, *i.e.*  
188 the PC input to the TCN network (**Fig 2b-c**) and (ii) raw pixel saliency *i.e.* the raw pixel input to the encoder network  
189 (**Supplementary Information**). The latter approach identifies the raw image pixels that contribute most to the eventual

Learning the rules of cell competition without prior scientific knowledge

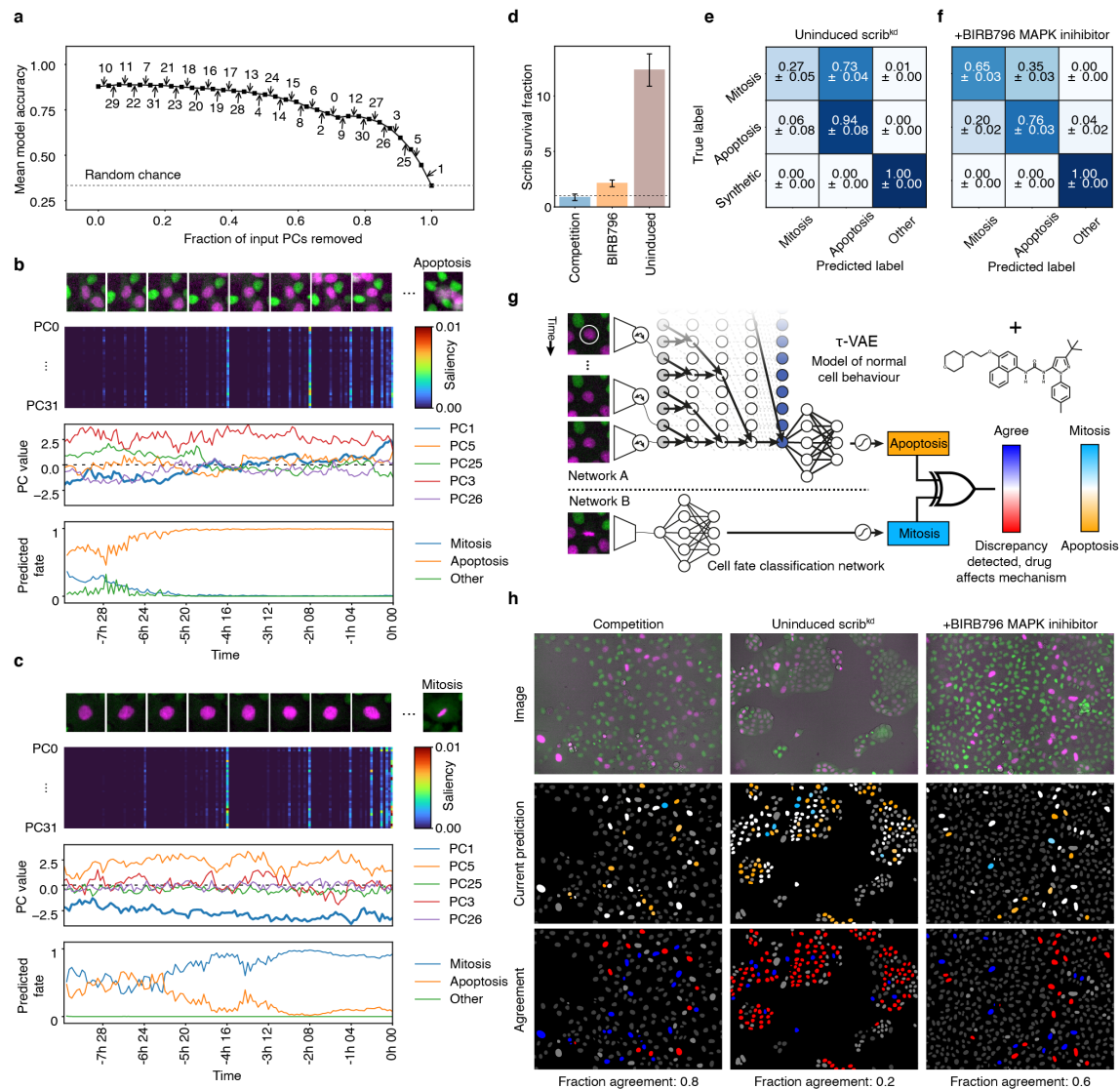


**Figure 2: An explainable internal representation of cell competition enables drug evaluation.** (a) Feature ablation demonstrates the role of each PC in the final prediction of the model. Each arrow indicates the cumulative replacement of a given PC with Gaussian noise. Error bars represent the standard deviation of model accuracy over all ten TCN models. (b) Example apoptotic trajectory with network predictions, and internal representation. Top row shows a sampled sequence of images from the trajectory. Second row shows the PC feature saliency over time calculated by the TCN. Third row is the values of the top-5 principal components over time. Final row is the prediction of cell fate over time. (c) Example mitotic trajectory with network predictions, and measured parameters, as in panel b. (d) Survival fraction for *scrib<sup>kd</sup>* cells in competition (MDCK<sup>WT</sup>:*scrib<sup>kd</sup>*), BIRB796 treated (MDCK<sup>WT</sup>:*scrib<sup>kd</sup>* + 2  $\mu$ M BIRB796) and uninduced (MDCK<sup>WT</sup>:*scrib<sup>kd, tet-</sup>*). Values below 1 (dotted line) indicate a cell population decrease, values greater than 1 indicate a population increase over the course of the experiment. (e) Confusion matrix of prediction accuracy for *scrib<sup>kd, tet-</sup>* cells ( $n = 161$  real trajectories) showing many mitoses are incorrectly predicted as apoptoses. (f) Confusion matrix for BIRB796 treated cells ( $n = 198$  real trajectories) showing a similar pattern to the *scrib<sup>kd, tet-</sup>* condition. (g) A discriminator network that uses two models to detect changes in cell behaviour. Network A is the  $\tau$ -VAE model of learned cell behaviour and Network B is the cell fate classification network. A discriminator (shown as an XOR gate) determines discrepancies between the two outputs. (h) Example of per-cell predictions and discriminator output for individual timepoints of competition, uninduced and BIRB796 treated timelapse movies, as in panel d. The top row shows the raw input image data. The middle row shows the current prediction (in this frame of the movie) of the  $\tau$ -VAE network for *scrib<sup>kd</sup>* cells in the FOV. Blue represents mitosis, orange represents apoptosis and white represents unknown fate or insufficient data to make a prediction at this time-point. The bottom row shows the discriminator output for each cell in the FOV. Red indicates that the  $\tau$ -VAE network did not agree with the fate classification, and blue indicates agreement. Grey cells have no predictions associated with them. The full movies can be found in the supplementary information.

190 prediction. The PC feature saliency reveals the timescales of activations within the network that are used to make  
191 predictions. The high gradients reveal that many of the late time steps are used in making the predictions for apoptosis  
192 and mitosis. Empirically, the pixel saliency reveals that nearby cells and the geometry (aspect ratio, convexity) of  
193 the nucleus (**Supplementary Information**) have significant contributions to the prediction - however, it is difficult to  
194 assign quantitative meaning to these observations, owing to the fact that they are in image space rather than feature  
195 space.

## 196 **Challenging the learned representation with biochemical perturbations**

197 Finally, to confirm that the network has learnt a model of mechanical cell competition, we sought to challenge the model  
198 with cells treated with different biochemical perturbations. For example, we performed experiments using cells that  
199 were uninduced (MDCK<sup>WT</sup>:scrib<sup>kd, tet-</sup>) such that there was no competition. In this case, the knockdown of the polarity  
200 protein Scribble is not induced with tetracycline (scrib<sup>kd, tet-</sup>), so the cells do not engage in mechanical competition  
201 with MDCK<sup>WT</sup> cells, but can still be distinguished by their H2B-RFP marker. We acquired timelapse data of the cells  
202 and confirmed that the scrib<sup>kd, tet-</sup> cell count was consistent with a non-competitive scenario (**Fig 2d, Supplementary**  
203 **Information**). From this dataset, we randomly selected a set of full length trajectories with a known fate (either  
204 apoptosis, mitosis or neither), and, after removing the final images and discarding the trajectories where no event occurs,  
205 we passed them to the  $\tau$ -VAE network. We found that the fate prediction accuracy of the network dropped significantly  
206 for the scrib<sup>kd, tet-</sup> cells. Strikingly, many scrib<sup>kd, tet-</sup> mitotic trajectories were incorrectly predicted to be apoptotic as can  
207 been seen from the confusion matrix (**Fig 2e**). This is an important result - the  $\tau$ -VAE, using the available information  
208 predicts, correctly, that the scrib<sup>kd, tet-</sup> cells should die under these conditions if knock-down of Scribble had been  
209 induced to start competition. A human would arrive at the same conclusion, given the same information. The fact that,  
210 under an unseen biochemical perturbation that disturbs the competition, we subsequently observe that they do not die,  
211 lays the foundation for a method to identify systematic deviations from normal (*i.e.* predictable) behavior.

212 This variation in the performance of the  $\tau$ -VAE when applied to cells under different biochemical perturbations  
213 suggested that our model is sensitive to changes in gene expression and the biochemical mechanisms of competition.  
214 Therefore, we sought to determine whether the methodology could be used for identifying drugs that perturb competition  
215 without further modification to the prediction network. Recent studies have suggested that p38 kinase inhibitors may  
216 interfere with mechanical cell competition by inhibiting the stress response pathways that lead to apoptosis [7]. To test  
217 this hypothesis, and to determine whether the network was able to discriminate these events, we acquired timelapse  
218 data of the cell competition (MDCK<sup>WT</sup>:scrib<sup>kd</sup>) in the presence of 2  $\mu$ M BIRB796, a p38 MAPK inhibitor [25]. We  
219 measured the loser cell count over the course of the experiments and noted that there was a higher survival fraction of  
220 the scrib<sup>kd</sup> cells, although they still grew significantly slower than MDCK<sup>WT</sup> (**Fig 2d, Supplementary Information**).  
221 From these data, we extracted single cell trajectories and used the  $\tau$ -VAE network to predict the fate of the cells as  
222 before. As with the uninduced dataset, the network predicted a significantly higher number of apoptoses where the true  
223 label was mitosis (**Fig 2f**).

224 Given that both the p38 MAPK inhibitor and the scrib<sup>kd, tet-</sup> condition interfere with the competition by limiting  
225 apoptosis, we would expect the scrib<sup>kd</sup> cells to reach higher densities in these conditions. Indeed, when analysing the  
226 network's representation, we noticed that the signatures of incorrectly predicted trajectories are more similar to the  
227 trajectories categorised as apoptotic under control conditions, especially with respect to the increased magnitude of  
228 PC1, that represents local cell density (**Supplementary Information**). This is consistent with the observations that the  
229 scrib<sup>kd, tet-</sup> and BIRB796 treated scrib<sup>kd</sup> cells reach higher densities, with significantly lower apoptotic rates. Overall,  
230 our results suggest that the  $\tau$ -VAE network, trained on the MDCK<sup>WT</sup>:scrib<sup>kd</sup> data, has learnt a complex and predictive  
231 model of cell competition, that is sensitive to local changes in the tissue organization and the signalling pathways  
232 participating in competition.

233 **A method for automated drug screening** Having established that the  $\tau$ -VAE network is able to represent a complex  
234 model of cell behavior in an explainable manner, we sought to define a general approach to utilise such a predictive  
235 model for image-based drug screening [26]. To do so, we introduce a novel discriminator network (**Fig 2g**) that  
236 compares the outputs of two models (Networks A & B) to determine discrepancies indicative of drug activity. The two  
237 networks utilise different amounts of information from each single-cell trajectory. Network A (the  $\tau$ -VAE), a model of  
238 "normal" cellular behavior, uses only the early part of the trajectory to predict the fate of the cell. In contrast, Network B  
239 (the cell fate classification network, **Supplementary Information**) uses the entire trajectory to classify the actual fate  
240 of the cell. When these two models agree for a particular cell, it suggests that the fate is predictable and thus competition  
241 conforms to learned behavior. However, when the two models disagree, this suggests that the cell is deviating from  
242 normal learned behavior, presumably due to the influence of an added drug or other perturbation. We demonstrate  
243 the utility of the discriminator to evaluate individual cells in movies in three different conditions, MDCK<sup>WT</sup>:scrib<sup>kd</sup>,  
244 MDCK<sup>WT</sup>:scrib<sup>kd, tet-</sup> and MDCK<sup>WT</sup>:scrib<sup>kd</sup> + 2  $\mu$ M BIRB796. First, we determined the performance of the cell fate

245 classification network, finding it to achieve an accuracy of 0.96 in determining cell fate ( $n = 392$ ) across all of the data.  
246 Then we used the  $\tau$ -VAE to make predictions for these cells, and the discriminator to determine the agreement with the  
247 cell fate classification network. In control conditions, the two networks show a high level of agreement with a fraction  
248 of agreement  $a$  of 0.8. The results show a similar pattern to the confusion matrices in **Fig 2e-f**, in that the uninduced  
249 Scribble ( $a=0.22$ ) and BIRB796 ( $a=0.62$ ) treated cells show the lowest fraction of agreement between the  $\tau$ -VAE  
250 and the cell fate classification, indicating deviation from the normal model of behavior. Therefore, the discriminator  
251 network automatically identifies conditions that deviate from learned behavior. Further, this approach can be utilized to  
252 monitor the time evolution and spatial pattern of predictions for individual cells in their original context (**Fig 2h**).

## 253 Conclusions

254 Deep learning is now a powerful tool in microscopy image analysis. However, the complex internal representations of  
255 many deep learning models, and the difficulty of analysing time dependent features, means that they have rarely been  
256 used to gain mechanistic insight into biological phenomena. Here, we developed an end-to-end machine learning model  
257 capable of discovering the physical parameters and rules of a complex biological phenomenon, cell competition, directly  
258 from image data. Starting *tabula rasa*, we demonstrate that our approach is able to learn a meaningful representation  
259 of cell behaviour in an automated and minimally-supervised manner. The model requires minimal human input to  
260 train and is able to correctly predict the fate of cells in mechanical cell competition. Strikingly, the model learns that  
261 local cell density is the single most important determinant of cell fate in mechanical competition, an observation that  
262 has taken scientists a decade of experimental research and data analysis to determine. Most exciting is that we are  
263 able to introspect the model to identify the physical features enabling prediction as well as the time-scale over which  
264 correct predictions are made. In the case of cell competition, we expect that these features will prove invaluable in  
265 formulating hypotheses about the nature of the mechanical changes detected during competition and the signalling  
266 pathways leading to loser cell death. This model can be used directly, and with no further modification, to investigate  
267 which candidate pathways participate in competition. Although we have demonstrated the utility of this approach using  
268 a model phenomenon and cell type, the approach is generalizable to many other systems, for example the study of the  
269 microenvironmental factors leading to differentiation of stem cells or embryonic development. Finally, we have shown  
270 that a novel discriminator network, based on the autonomously learned  $\tau$ -VAE model, can detect conditions which  
271 deviate from the normal cellular behaviour due to inhibition or silencing, signifying that it can be used as a screening  
272 tool. Once trained, this fully automated system is able to discriminate between normal cell behavior and perturbations  
273 without any further human intervention, paving the way for mechanism-aware AI-based drug discovery.

## 274 Methods

275 **Cell culture, imaging assays, single-cell tracking and cell fate classification network** Detailed methods can be  
276 found in the supplementary information.

277 **Drug treatments** BIRB796 (Tocris 5989, [25]) was dissolved in DMSO and added to the cell culture 5 h before  
278 imaging at a final concentration of 2  $\mu$ M. As a negative control, a similar volume of DMSO was added to some wells.

279 **Variational Autoencoder ( $\beta$ -VAE)** We built a convolutional variational autoencoder to learn a low-dimensional  
280 representation of the cell image data that could be used by a TCN for fate prediction. The encoder network consists of  
281 four convolutional layers with  $3 \times 3$  kernels, Swish activations, with 32, 64, 128 and 256 kernels respectively. Each  
282 layer was pooled by a  $2 \times 2$  max-pooling operation. The convolutional output was flattened and split into two arms  
283 with two fully connected layers for the  $\mu$  and  $\sigma^2$  estimators. We found that adding additional fully connected layers of  
284 128 units between the estimators and the flattened encoder output improved the model performance. We used a random  
285 normal sampler to generate samples from the distribution. The decoder is inverse of the encoder, using nearest neighbor  
286 upsampling between the convolutional layers.

287 We use the revised objective function [21, 27] to train the network:

$$\mathcal{L}(\theta, \phi; \mathbf{x}, \mathbf{z}, \gamma, C) = \mathbb{E}_{q_{\phi}(\mathbf{z}|\mathbf{x})}[\log p_{\theta}(\mathbf{x}|\mathbf{z})] - \gamma |\mathbf{D}_{\text{KL}}(q_{\phi}(\mathbf{z}|\mathbf{x}) || p(\mathbf{z})) - C| \quad (1)$$

288 Our loss function is composed of two terms. The first term is the reconstruction loss term which penalises differences  
289 between the reconstruction (the decoded, encoded input) and the real input. In practice, we use the mean squared error  
290 between the input image ( $\mathbf{x}$ ) and the output ( $\mathbf{x}'$ ) of the  $\beta$ -VAE. The second term is the Kullback-Leibler divergence  
291 ( $\mathbf{D}_{\text{KL}}(\cdot || \cdot)$ ), which penalizes the latent space model variance from dropping to zero, by forcing the encoding to match



292 the Gaussian prior with a diagonal covariance matrix,  $N(0, I)$ . This has the effect of regularizing the latent space to  
293 promote a continuous representation of the underlying image data.

294 In our implementation, we dynamically adjust the bottleneck capacity ( $C$ ) of the network during training. The value  
295 of  $C$  is scaled linearly as a function of training iteration, reaching a maximum value  $C_{\max}$ . This ensures that at early  
296 training iterations the network prioritizes the encoding, while at later iterations this is refined to optimize the decoding.  
297 The scaling constant  $\gamma$  balances the two terms of the loss function.

298 We prepared a training set of 1.2 million images of cells by sampling individual cells from the time-lapse movies. A  
299 fraction of cells (random 10% of cells in frame) was selected from a random sample of frames (10% of frames in movie)  
300 and an ROI of varying size around each cell was extracted. These were then downsampled using nearest neighbor  
301 sampling, to the network input size of  $(64 \times 64 \times 2)$ . We then trained the  $\beta$ -VAE network using  $\gamma = 1000$ ,  $C_{\max} = 50$ ,  
302 latent vector  $\mathbf{z} \in \mathbb{R}^n$ . We found  $n = 32$  to be the optimal value of the latent space dimensions. Optimization was  
303 performed using an Adam optimizer for 100 epochs and a minibatch size of 256. Training images were augmented  
304 *on-the-fly* by random flipping, rotations and simulated edge cropping.

305 **Trajectory Synthesis** In order to simulate a third class of trajectory, referred to as “synthetic”, we utilised the  
306 generative property of the decoder network. The first frame of each synthetic trajectory is a real image, i.e. it is decoded  
307 by the decoder network from the latent-space encoding of an image that actually exists. For the next frame, the encoding  
308 is adjusted by adding to each latent variable a scalar that is sampled from a Gaussian distribution (with  $\mu = 0.0$  and  
309  $\sigma = 0.2$ ). The image for this second frame is then the decoder output with this new encoding as input. This process is  
310 then repeated until all the frames of the synthetic movie are generated, with the trajectories taking a random walk in  
311 latent space.

312 **Principal Component Analysis (PCA)** We used PCA to analyse the learnt representation of the total dataset. The  
313 principal components of the latent features derived by the  $\beta$ -VAE have a higher degree of interpretability than the latent  
314 features themselves. PCA was applied to the latent features before analysis of the latent space was undertaken. We used  
315 the *PCA* function from *Scikit-learn* to perform the decomposition into 32 components, once for each of the  $\beta$ -VAE  
316 latent dimensions.

317 **Temporal Convolution Network (TCN)** The timelapse sequences encoded by the  $\beta$ -VAE become the input features  
318 ( $n \times t$ ) of a temporal convolution network (TCN) [22]. The procedure for preparing a timelapse movie for input to the  
319 TCN is as follows. First, each frame in the timelapse movie is normalized such that the pixel values of that individual  
320 frame have zero mean and unit variance. This is performed on a per-channel basis, such that the RFP and GFP channels  
321 are normalized separately. Next, the normalized timelapse movie is fed through the encoder network of the trained  
322  $\beta$ -VAE. The encoder yields three outputs for each latent variable - the mean, standard deviation, and Gaussian-sampled  
323 value. This is calculated for every timelapse movie in the dataset.

324 Once encoded, the timelapse sequences are transformed from latent space ( $\mathbf{Z}$ ) into principal component space ( $\mathbf{T}$ ) using  
325 the transform  $\mathbf{T} = \mathbf{Z}\mathbf{W}$ , where  $\mathbf{W}$  are the principal components. and then fed into the TCN for training. The TCN is  
326 formed of seven convolutional layers with respective dilations of 1, 2, 4, 8, 16, 32 and 64. Each of these layers has 64  
327 convolutional filters. The output from the convolutional layers is fed into a fate prediction head. This network projects  
328 the output into a classification, and is composed of a fully connected layer with 128 units, and a final fully connected  
329 layer with three units that represent the possible classifications of the sequence ("apoptosis", "mitosis" or "synthetic").  
330 We used a sparse categorical cross entropy loss function to train the network.

331 The TCN is trained with a batch size of 128 for 100 epochs. Optimization was performed using the RMSprop optimizer  
332 with a learning rate of 0.001. Training sequences were augmented *on-the-fly* by random frame removal, cropping and  
333 the addition of noise to the encoded sequences. Regularization was ensured by applying batch normalization and a  
334 dropout rate of 0.3 to the TCN layer of the network.

335 **Feature saliency** We can determine the salient features of the input images by calculating a saliency map ( $M_c$ ) for  
336 an input ( $x$ ). This is achieved by calculating the gradient of the output function  $S_c$  with respect to the input during  
337 backpropagation:  $M_c(x) = \partial S_c(x) / \partial x$ . In practice, we average  $n$  gradient calculations, each with a small added  
338 Gaussian noise ( $\mu=0.0$ ,  $\sigma = 0.1 \times |(\max(S_c) - \min(S_c))|$ ) component to the input.

339 **Software availability** A reference implementation of the  $\tau$ -VAE is available at: [https://github.com/](https://github.com/lowe-lab-ucl/cellx-predict)  
340 [lowe-lab-ucl/cellx-predict](https://github.com/lowe-lab-ucl/cellx-predict)

341 **Data availability** Data is available from the UCL data repository: <https://dx.doi.org/10.5522/04/16578959>.

## 342 Author contributions

343 ARL and GC conceived and designed the research. GV performed experiments. CJS developed and performed  
344 computational analysis. ARL wrote the image processing and cell tracking code. CJS, GV, GC and ARL evaluated the  
345 results and wrote the paper.

## 346 Acknowledgments

347 This work was supported by a BBSRC LIDo AI PhD studentship to CJS. GV was supported by BBSRC grant  
348 BB/S009329/1. We thank Nathan Day, Jasmine Michalowska and Dan Smaje for help annotating data. We also thank  
349 members of the Lowe and Charras labs for discussions and technical support during the project. ARL wishes to  
350 acknowledge the Turing Fellowship from the Alan Turing Institute. ARL and GC wish to acknowledge the support of  
351 BBSRC grant BB/S009329/1.

## 352 References

- 353 [1] R. Levayer and E. Moreno, “Mechanisms of cell competition: Themes and variations,” *The Journal of Cell Biology*, vol. 200,  
354 no. 6, pp. 689–698, 2013.
- 355 [2] G. Morata and P. Ripoll, “Minutes: mutants of drosophila autonomously affecting cell division rate,” *Dev. Biol.*, vol. 42,  
356 pp. 211–221, Feb 1975.
- 357 [3] T. Parker, E. Madan, K. Gupta, E. Moreno, and R. Gogna, “Cell competition spurs selection of aggressive cancer cells,” *Trends*  
358 *in Cancer*, vol. 6, pp. 732–736, sep 2020.
- 359 [4] R. Levayer, B. Hauert, and E. Moreno, “Cell mixing induced by myc is required for competitive tissue invasion and destruction,”  
360 *Nature*, vol. 524, pp. 476 EP–, 08 2015.
- 361 [5] J.-P. Vincent, A. G. Fletcher, and L. A. Baena-Lopez, “Mechanisms and mechanics of cell competition in epithelia,” *Nature*  
362 *Reviews Molecular Cell Biology*, vol. 14, pp. 581 EP–, 08 2013.
- 363 [6] C. Hogan, S. Dupré-Crochet, M. Norman, M. Kajita, C. Zimmermann, A. E. Pelling, E. Piddini, L. A. Baena-López, J.-P.  
364 Vincent, Y. Itoh, H. Hosoya, F. Pichaud, and Y. Fujita, “Characterization of the interface between normal and transformed  
365 epithelial cells,” *Nature Cell Biology*, vol. 11, pp. 460 EP–, 03 2009.
- 366 [7] L. Wagstaff, M. Goschorska, K. Kozyska, G. Duclos, I. Kucinski, A. Chessel, L. Hampton-O’Neil, C. R. Bradshaw, G. E.  
367 Allen, E. L. Rawlins, P. Silberzan, R. E. Carazo Salas, and E. Piddini, “Mechanical cell competition kills cells via induction of  
368 lethal p53 levels,” *Nature Communications*, vol. 7, pp. 11373 EP–, 04 2016.
- 369 [8] A. Bove, D. Gradeci, Y. Fujita, S. Banerjee, G. Charras, and A. R. Lowe, “Local cellular neighborhood controls proliferation in  
370 cell competition,” *Molecular Biology of the Cell*, vol. 28, no. 23, pp. 3215–3228, 2017. PMID: 28931601.
- 371 [9] D. Gradeci, A. Bove, G. Vallardi, A. R. Lowe, S. Banerjee, and G. Charras, “Cell-scale biophysical determinants of cell  
372 competition in epithelia,” *eLife*, vol. 10, May 2021.
- 373 [10] E. Ren, S. Kim, S. Mohamad, S. F. Huguet, Y. Shi, A. R. Cohen, E. Piddini, and R. C. Salas, “Deep learning-enhanced  
374 morphological profiling predicts cell fate dynamics in real-time in hPSCs,” *bioRxiv*, aug 2021.
- 375 [11] D. P. Kingma and M. Welling, “Auto-encoding variational bayes,” 2013. cite arxiv:1312.6114.
- 376 [12] C. K. Chan, A. Hadjitheodorou, T. Y.-C. Tsai, and J. A. Theriot, “Quantitative comparison of principal component analysis and  
377 unsupervised deep learning using variational autoencoders for shape analysis of motile cells,” *bioRxiv*, jun 2020.
- 378 [13] A. Zaritsky, A. R. Jamieson, E. S. Welf, A. Nevarez, J. Cillay, U. Eskiocak, B. L. Cantarel, and G. Danuser, “Interpretable deep  
379 learning uncovers cellular properties in label-free live cell images that are predictive of highly metastatic melanoma,” *Cell*  
380 *Systems*, vol. 12, pp. 733–747.e6, jul 2021.
- 381 [14] Z. Wu, B. B. Chhun, G. Popova, S.-M. Guo, C. N. Kim, L.-H. Yeh, T. Nowakowski, J. Zou, and S. B. Mehta, “DynaMorph:  
382 self-supervised learning of morphodynamic states of live cells,” *bioRxiv*, jul 2020.
- 383 [15] K. D. Yang, K. Damodaran, S. Venkatachalapathy, A. C. Soylemezoglu, G. V. Shivashankar, and C. Uhler, “Predicting cell  
384 lineages using autoencoders and optimal transport,” *PLOS Computational Biology*, vol. 16, p. e1007828, apr 2020.
- 385 [16] F. Buggenthin, F. Buettner, P. S. Hoppe, M. Endeke, M. Kroiss, M. Strasser, M. Schwarzfischer, D. Loeffler, K. D. Kokkaliaris,  
386 O. Hilsenbeck, T. Schroeder, F. J. Theis, and C. Marr, “Prospective identification of hematopoietic lineage choice by deep  
387 learning,” *Nature Methods*, vol. 14, pp. 403–406, feb 2017.
- 388 [17] M. Norman, K. A. Wisniewska, K. Lawrenson, P. Garcia-Miranda, M. Tada, M. Kajita, H. Mano, S. Ishikawa, M. Ikegawa,  
389 T. Shimada, and Y. Fujita, “Loss of scribble causes cell competition in mammalian cells,” *Journal of Cell Science*, vol. 125,  
390 no. 1, pp. 59–66, 2012.
- 391 [18] O. Ronneberger, P. Fischer, and T. Brox, “U-net: Convolutional networks for biomedical image segmentation,” *CoRR*,  
392 vol. abs/1505.04597, 2015.

Learning the rules of cell competition without prior scientific knowledge

---

- 393 [19] K. Ulicna, G. Vallardi, G. Charras, and A. R. Lowe, “Automated deep lineage tree analysis using a Bayesian single cell tracking  
394 approach,” *Frontiers in Computer Science*, sep 2021.
- 395 [20] V. Mnih, N. Heess, A. Graves, and k. kavukcuoglu, “Recurrent models of visual attention,” in *Advances in Neural Information  
396 Processing Systems* (Z. Ghahramani, M. Welling, C. Cortes, N. Lawrence, and K. Q. Weinberger, eds.), vol. 27, Curran  
397 Associates, Inc., 2014.
- 398 [21] I. Higgins, L. Matthey, A. Pal, C. Burgess, X. Glorot, M. Botvinick, S. Mohamed, and A. Lerchner, “beta-vae: Learning basic  
399 visual concepts with a constrained variational framework,” in *5th International Conference on Learning Representations, ICLR  
400 2017, Toulon, France, April 24-26, 2017, Conference Track Proceedings*, 2017.
- 401 [22] A. van den Oord, S. Dieleman, H. Zen, K. Simonyan, O. Vinyals, A. Graves, N. Kalchbrenner, A. Senior, and K. Kavukcuoglu,  
402 “Wavenet: A generative model for raw audio,” *arXiv*, 2016.
- 403 [23] R. Levayer, C. Dupont, and E. Moreno, “Tissue crowding induces caspase-dependent competition for space,” *Current Biology*,  
404 vol. 26, pp. 670–677, mar 2016.
- 405 [24] D. Smilkov, N. Thorat, B. Kim, F. B. Viégas, and M. Wattenberg, “Smoothgrad: removing noise by adding noise,” *CoRR*,  
406 vol. abs/1706.03825, 2017.
- 407 [25] Y. Kuma, G. Sabio, J. Bain, N. Shpiro, R. Márquez, and A. Cuenda, “BIRB796 inhibits all p38 MAPK isoforms in vitro and in  
408 vivo,” *Journal of Biological Chemistry*, vol. 280, pp. 19472–19479, may 2005.
- 409 [26] S. N. Chandrasekaran, H. Ceulemans, J. D. Boyd, and A. E. Carpenter, “Image-based profiling for drug discovery: due for a  
410 machine-learning upgrade?,” *Nature Reviews Drug Discovery*, vol. 20, pp. 145–159, dec 2020.
- 411 [27] C. P. Burgess, I. Higgins, A. Pal, L. Matthey, N. Watters, G. Desjardins, and A. Lerchner, “Understanding disentangling in  
412  $\beta$ -vae,” 2018.

